

Fast Sideband Control of a Weakly Coupled Multimode Bosonic Memory

Jordan Huang,^{1,*} Thomas J. DiNapoli,¹ Gavin Rockwood,¹ Ming Yuan,² Prathyankara Narasimhan,¹ Eesh Gupta,³ Mustafa Bal,⁴ Francesco Crisa,⁴ Sabrina Garattoni,⁴ Yao Lu,⁴ Liang Jiang,² and Srivatsan Chakram^{1,†}

¹*Department of Physics and Astronomy, Rutgers University, Piscataway, NJ 08854, USA*

²*Pritzker School of Molecular Engineering, University of Chicago, Chicago, Illinois 60637, USA*

³*Department of Applied Physics, Stanford University, Stanford, California 94305, USA*

⁴*Superconducting Quantum Materials and Systems Division,*

Fermi National Accelerator Laboratory (FNAL), Batavia, IL 60510, USA

(Dated: March 14, 2025)

Circuit quantum electrodynamics (cQED) with superconducting cavities coupled to nonlinear circuits like transmons offers a promising platform for hardware-efficient quantum information processing. A critical challenge is developing control protocols that mitigate cavity errors arising from ancilla-induced decoherence, nonlinearities, and crosstalk. We address this by weakening the dispersive coupling while also demonstrating fast, high-fidelity multimode control by dynamically amplifying gate speeds through transmon-mediated sideband interactions. This approach enables transmon-cavity SWAP gates, for which we achieve speeds up to 30 times larger than the bare dispersive coupling. Combined with transmon rotations, this allows for efficient, universal state preparation in a single cavity mode, though achieving unitary gates and extending control to multiple modes remains a challenge. In this work, we overcome this by introducing two sideband control strategies: (1) a shelving technique that prevents unwanted transitions by temporarily storing populations in sideband-transparent transmon states and (2) a method that exploits the dispersive shift to synchronize sideband transition rates across chosen photon-number pairs to implement transmon-cavity SWAP gates that are selective on photon number. We leverage these protocols to prepare Fock and binomial code states across any of ten modes of a multimode cavity with millisecond cavity coherence times. We demonstrate the encoding of a qubit from a transmon into arbitrary vacuum and Fock state superpositions, as well as entangled NOON states of cavity mode pairs—a scheme extendable to arbitrary multimode Fock encodings. Furthermore, we implement a new binomial encoding gate that converts arbitrary transmon superpositions into binomial code states in $4\ \mu\text{s}$ (less than $1/\chi$), achieving an average post-selected final state fidelity of 96.3% across different fiducial input states. By using precalibrated transmon and sideband pulses, our work demonstrates multimode control with significantly reduced calibration requirements, enabling efficient unitary operations using sideband interactions in multimode cQED systems.

I. INTRODUCTION

Superconducting cavities coupled to nonlinear, ancillary circuits form a promising platform for quantum computing based on circuit quantum electrodynamics (cQED) [1]. This architecture leverages the superconducting circuit’s nonlinearity to manipulate quantum information stored in high-coherence cavity modes [2]. When coupled to a multimode cavity, this architecture also allows multiplexed control of many cavity modes with only a few control lines [3, 4]. Universal control of a harmonic oscillator has been realized through a variety of control schemes [5, 6]. These control schemes have been extended to multiple oscillators to demonstrate entanglement [7, 8] and gate operations between multiple cavity modes, using both fixed-frequency transmons [9, 10] and tunable coupler circuits [11, 12]. The harmonic oscillator’s expanded Hilbert space and straightforward decoherence mechanisms—primarily photon loss—have also enabled demonstrations of hardware-efficient quantum error correction (QEC) using bosonic codes [13–17].

The dispersive coupling to a nonlinear circuit, while crucial for implementing universal cavity control, introduces ancilla-mediated errors that are frequently the dominant error channels. In particular, the cavity modes inherit decay from the lossy, nonlinear circuit through the inverse-Purcell effect, setting a fundamental upper bound on cavity coherence—an effect that becomes increasingly significant as cavity lifetimes are extended [18–21]. In multimode architectures, the always-on dispersive interaction and the nonlinearities inherited by the cavity modes introduce coherent crosstalk between modes [22], further contributing to gate infidelity and placing constraints on the scalability of these systems.

One approach to mitigating these challenges is to weaken the dispersive interaction, thereby reducing the magnitude of ancilla-mediated errors. However, this reduction in interaction strength also slows gate speeds in traditional control schemes that rely on photon-number-selective ancilla rotations [5, 8, 23, 24]. To address this trade-off, control strategies utilizing conditional cavity displacements have been developed. In these schemes, interaction rates are enhanced beyond the bare dispersive coupling by using large cavity displacements as an interaction switch [6, 25]. Another method for increasing gate speeds beyond the dispersive coupling strength

* jah499@scarletmail.rutgers.edu

† schakram@physics.rutgers.edu

is to use ancilla displacements to activate charge-driven sideband interactions [19]. The transmon's quartic non-linearity can activate various parametric processes [26], such as cavity beamsplitters [27, 28] and transmon-mode SWAP gates using two drive photons [29]. The fastest transmon-mediated sideband interaction for a given drive strength uses a single drive photon to convert two transmon excitations into a single photon in a coupled cavity mode [9, 30].

We use such charge-driven sidebands to realize a tunable Jaynes–Cummings interaction (within the transmon's $|g\rangle$ - $|f\rangle$ manifold) between the transmon and any target mode of a multimode cavity. Here, the coupling is modulated by the strength of the transmon drive. When combined with transmon rotations, this enables efficient, universal state preparation using the Law–Eberly protocol [31]—originally developed to control the motional states of trapped ions [32] and later demonstrated in superconducting circuits [33]. This protocol reverses the sequence that brings the target state to the vacuum one photon at a time and has a sequence length sub-linear in the maximum photon number of the target state. However, incommensurate sideband interaction rates across different photon-number states from the \sqrt{n} bosonic enhancement pose significant challenges in implementing arbitrary gate operations [34]. Furthermore, calibrating the arbitrary transmon and sideband rotation angles required for a given unitary can be challenging, especially in the presence of large Stark shifts. This difficulty is analogous to that encountered when realizing target unitaries via optimal control pulses generated through algorithms such as GRAPE [5, 35]. In traditional dispersive control [23] or with conditional displacement gates [6], employing discrete families of pulses that can be independently calibrated and optimized offers advantages in both ease of implementation and robustness against classical control errors and quantum state-dependent shifts [36, 37].

In this work, we overcome these challenges by introducing two sideband control strategies: the first is a shelving technique that temporarily stores populations in the transmon $|e\rangle$ state so that they remain unaffected by sideband drives. The second method implements photon-number-selective sideband operations by matching sideband rates across chosen photon numbers, using the sideband drive detuning as a control knob. Using these strategies, we introduce a method of state preparation and unitary synthesis that is implemented through a discrete set of precalibrated transmon and sideband pulses. Using these techniques, we prepare binomial code states [38] across ten cavity modes in approximately 1 μ s. We also implement unitary operations that encode a qubit from the transmon into vacuum and Fock state superpositions, as well as into entangled NOON states between chosen cavity mode pairs. Finally, we implement a new encoding unitary that transfers a transmon superposition into a binomial logical qubit in any target mode at a rate exceeding the dispersive shift. We demon-

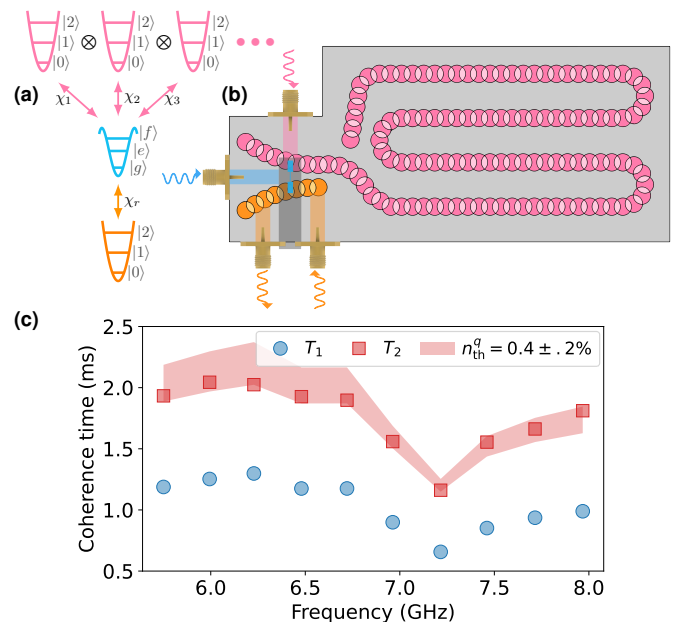


FIG. 1. **Multimode bosonic memory device.** (a) Device architecture and (b) schematic depicting the multimode cavity-based quantum processor [4, 8] comprised of a multimode cavity (pink) with cavity modes coupled to and controlled by a single transmon circuit (blue), which is measured using a readout cavity (orange). The cavities are fabricated using the flute method [4, 8], by drilling offset, overlapping, evanescent holes in a monolithic block of high-purity (5N5) aluminum. The hole locations are indicated in the schematic. (c) The measured coherence times of the storage cavity modes. The shaded regions indicate the inferred qubit thermal population that would give rise to the measured cavity T_2 .

strate these multimode operations on a cavity memory with ten active modes with a weak dispersive coupling to a transmon ancilla. In this regime, we achieve SWAP operations that are 30 times faster than the bare dispersive coupling.

II. MULTIMODE BOSONIC MEMORY

Our system architecture and device schematic are shown in Fig. 1(a) and (b). The device features a multimode rectangular waveguide cavity supporting several high-coherence modes, each with lifetimes ranging from 0.6–1.3 ms, as shown in Fig. 1(c). The cavity is fabricated from a monolithic block of high-purity (5N5) aluminum using the flute method, where the cavity volume is formed by drilling offset, overlapping, evanescent holes [4]. The mode spectrum is set by the cavity dimensions, with the lowest mode around 5.75 GHz. We realize a nearly evenly spaced mode spectrum, with separations of approximately 250 MHz, by tapering the cavity height. The transmon is inserted at the taller end of the cavity

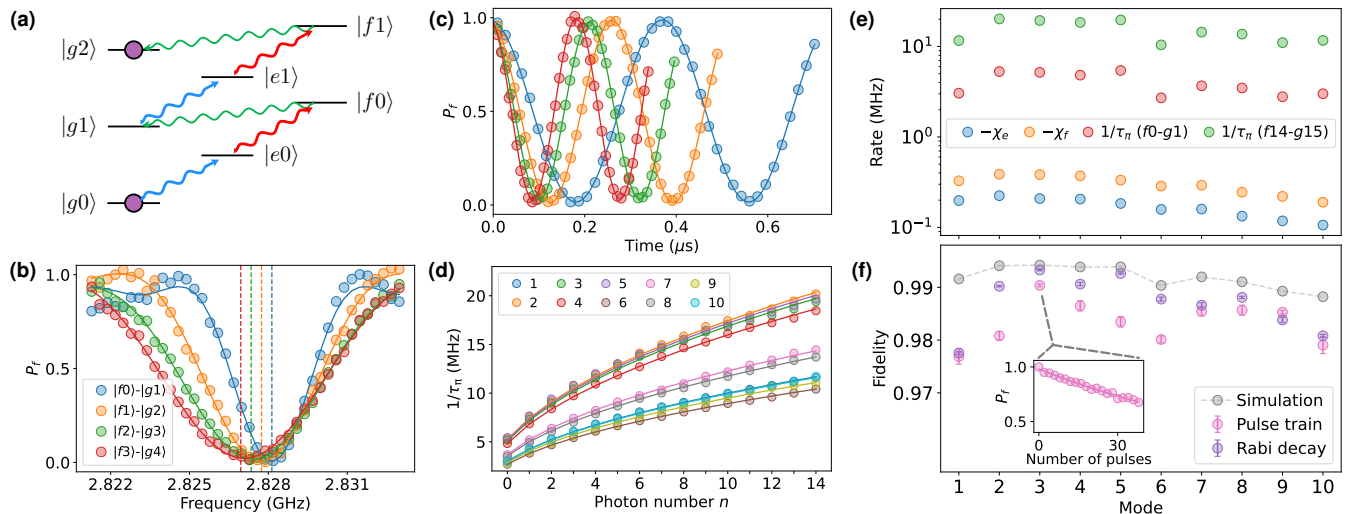


FIG. 2. **Charge-driven sideband interactions in the multimode memory.** (a) Energy level diagram for a transmon and a single cavity mode illustrating how to climb the levels with transmon rotations (blue and red) and $|f, n\rangle$ - $|g, n+1\rangle$ sideband transitions (green). (b) Spectroscopy and (c) and stimulated vacuum Rabi oscillations of $|f, n\rangle$ - $|g, n+1\rangle$ transitions for mode 3 of the storage cavity. (d) Sideband Rabi oscillation rate as a function of photon number for the first ten modes of the multimode memory, up to a photon number of $n = 14$. (e) Comparison of the maximum achieved SWAP rate for the $|f0\rangle$ - $|g1\rangle$ and $|f13\rangle$ - $|g14\rangle$ transitions against the bare dispersive interaction strengths for the $|e\rangle$ and $|f\rangle$ states. (f) The pink markers show the $|f0\rangle$ - $|g1\rangle$ SWAP fidelities inferred from a pulse train experiment. The data is fit to an exponential decay as a function of pulse number to extract the fidelity. The purple markers show the $|f0\rangle$ - $|g1\rangle$ SWAP fidelities inferred from fitting the $|f0\rangle$ - $|g1\rangle$ oscillations to an effective Rabi model as in [12]. The grey markers show the sideband interaction fidelities extracted from Lindblad master equation simulations.

with transmon-mode couplings chosen to realize dispersive shifts of $\chi \approx 100$ – 200 kHz. With the transmon's $T_1 \approx 56$ μ s, this leads to an inverse-Purcell limit of about 60 ms for the coherence times of the cavity modes due to their coupling to the lossier transmon. The transmon frequency is $f_q = 4.606$ GHz, its dephasing time is $T_2 \approx 66$ μ s, and the thermal population is 0.3 ± 0.1 %. The transmon is also coupled to a separate flute-style cavity whose fundamental mode at $f_r = 8.067$ GHz is used for transmon readout. In addition to readout input and output drives, the system has direct transmon and multimode storage cavity drive lines.

III. FAST CHARGE-DRIVEN SIDEBAND INTERACTIONS

The quartic nonlinearity of the transmon mediates a sideband interaction between the states $|f, n\rangle$ and $|g, n+1\rangle$, where n is the number of photons in the target cavity mode [39]. This interaction is initiated by applying a charge drive on the transmon at the frequency difference between its $|f\rangle$ state and the cavity mode. While these states do not directly couple, an interaction is facilitated through virtual states which are coupled to $|f, n\rangle$ and $|g, n+1\rangle$ through the dressing from the transmon drive and the Jaynes–Cummings coupling with the target

cavity mode (the virtual states being $\{|e, n\rangle, |e, n+1\rangle\}$ for small drive amplitudes). The resulting sideband interaction can be described as $g_{\text{sb},i} (|g\rangle \langle f| b_i^\dagger + |f\rangle \langle g| b_i)$, where b_i is the lowering operator for photons in cavity mode i . Its interaction rate, computed to lowest order in the nonlinearity, without making a rotating wave approximation for the transmon displacement, is given by

$$g_{\text{sb},i} = \frac{\sqrt{2}(\omega_q + K + \Delta_i)}{2\omega_q + K + \Delta_i} \frac{\epsilon}{g_i} \chi_i \approx \frac{\epsilon}{\sqrt{2}g_i} \chi_i. \quad (1)$$

Here, ω_q is the transmon's $|g\rangle$ - $|e\rangle$ frequency, K is its anharmonicity, $\Delta_i = \omega_q - \omega_{c,i}$ is the transmon-mode detuning, g_i is the bare transmon-mode coupling, and χ_i is the dispersive shift of the transmon $|e\rangle$ state from addition of a photon in mode i . In this form, it is clear that the sideband interaction can be enhanced beyond χ with a strong drive ϵ . Higher-order corrections to the sideband rate are discussed in Section S3 B of the Supplementary Information.

In conjunction with transmon rotations, the sideband interaction allows us to climb the ladder of Fock levels of any cavity mode, as schematically illustrated in the level diagram shown in Figure 2(a). We measure the resonance frequency of the $|f, n\rangle$ - $|g, n+1\rangle$ transition by performing sideband spectroscopy measurements after preparing the transmon in the $|f\rangle$ state. We start with the cavity in the

ground state and locate the $|f, 0\rangle$ - $|g, 1\rangle$ resonance. Next, we sweep the pulse duration to identify the π -pulse time corresponding to adding a single photon in the target cavity mode. This implements a transmon-cavity SWAP gate. The process is iteratively repeated for higher photon numbers, identifying the $|f, n\rangle$ - $|g, n+1\rangle$ transitions and extracting the corresponding π pulse times (shown in Figure 2(b) and (c)). We observe that the resonance frequency of the n -photon sideband is offset by $n\chi_f$ due to the dispersive shift of the $|f\rangle$ state. Additionally, the interaction rates exhibit a \sqrt{n} bosonic enhancement with photon number as shown in Figure 2(d). Figure 2(e) compares the rate of the $|f, 0\rangle$ - $|g, 1\rangle$ SWAP gate to the dispersive interaction (χ_e, χ_f) of the modes. We achieve SWAP gate times nearly 30 times faster than χ_e by using strong transmon drive strengths ranging from 0.1–1.3 GHz. At these drive strengths, the transition frequency has a significant drive-amplitude-dependent Stark shift (approximately 10–50 MHz). Here, the Floquet modes adiabatically connected to the undriven transmon states have significant support with higher transmon levels. To maximize the interaction fidelity, we use a smooth ramp (bump function) that is slow enough to allow adiabatic evolution of the undriven states to their corresponding Floquet modes and fast enough to induce high-fidelity population exchange. This corresponds to the ramp initializing the initial state into an equal superposition of Floquet modes at the final drive amplitude through a Landau-Zener-like transition (see Section S7 of the Supplementary Information).

We characterize the fidelity of the sideband SWAP gate using an error amplification experiment where we measure the $|f\rangle$ state population following a train of $|f0\rangle$ - $|g1\rangle$ π -pulses. An optimally calibrated sideband pulse results in a nearly exponential decay of the population, as shown in the inset of Fig. 2(f), whereas calibration errors lead to non-exponential behavior due to coherent over- or under-rotations. We fit the exponential decay to extract a pulse fidelity, which includes errors from decoherence and leakage to higher transmon levels. To isolate the contribution of decoherence alone, we fit the decay of a long-time sideband Rabi oscillation to an effective Rabi decay model [12]. The fidelities extracted from both pulse train and Rabi decay measurements are shown in Fig. 2(f), along with a comparison with master equation simulations. The pulse-train fidelities range from approximately 97.5–99% and are found to be marginally lower than the Rabi decay fidelity, attributed to residual leakage errors caused by imperfections in the pulse ramps. The fidelities from Rabi decay are found to be consistent with master equation simulations that account for transmon and cavity decay and dephasing. In addition to decoherence and leakage errors, the pulses used in the gate protocols are susceptible to coherent errors arising from calibration drifts during the measurements. These drifts are attributed to drive-amplitude fluctuations, which lead to frequency errors due to the large Stark shifts. We mitigate this by performing iterative cal-

ibrations of the sideband frequencies and π -pulse times for all target photon numbers before each experiment. We detail the procedure followed to calibrate and characterize the sideband pulses in Section S4 of the Supplementary Information. At sufficiently high sideband drive strengths, which vary between modes, fidelities degrade due to transmon ionization [40], imposing a fundamental limit on gate speed. To avoid this, we constrain the drive strength below this threshold.

We also measure the thermal population of the cavity modes by using a new sideband-based protocol that extends the standard protocol used for transmon thermal population measurements [41]. This is estimated by comparing the contrast of $|f0\rangle$ - $|g1\rangle$ sideband rotations with and without initially preparing the transmon in $|f\rangle$, yielding cavity-mode thermal populations in the range of 0.3–2%. To further reduce thermal excitations, we implement transmon reset using the $|f0\rangle$ - $|g1\rangle$ sideband with our readout resonator, which has a short lifetime of approximately 600 ns. Combined with sidebands to the storage modes, we implement a sequential sideband reset protocol applicable to any storage mode. In this protocol, detailed in Section S6 of the Supplementary Information, the cavity state is reset one photon at a time by shuttling photons to the transmon $|f\rangle$ state and removing it through the readout mode. This increases our experimental repetition rate by two orders of magnitude (7 ms to 50 μ s) and cools the cavity modes to a thermal population of 0.2–0.7%, consistent with the expected thermal population of our readout resonator, as inferred from transmon dephasing.

IV. SINGLE-MODE SIDEBAND CONTROL

We demonstrate single-mode control over any cavity mode by preparing both Fock states $|n\rangle$ and vacuum-Fock superpositions $\frac{|0\rangle+|n\rangle}{\sqrt{2}}$ by climbing the Jaynes-Cummings ladder with transmon rotations and sideband pulses. Fock states are prepared using a sequence of broadband π_{ge} and π_{ef} pulses followed by $|f, n\rangle$ - $|g, n+1\rangle$ sideband π pulses. To achieve superposition states, we employ our *shelving* method—temporarily storing part of the state in the $|e\rangle$ manifold, which is transparent to the $|f, n\rangle$ - $|g, n+1\rangle$ sidebands. We track the evolution of each component throughout the sequence, arranging it so that only one component is selectively transferred via sideband transitions while the others remain unaffected. Without shelving, the components would evolve at different rates due to the incommensurate sideband interaction rates across different photon numbers. Figure 3(a) shows the pulse sequence used to prepare the superposition state $\frac{|0\rangle+|2\rangle}{\sqrt{2}}$, with shelving pulses indicated by blue underlines. Figure 3(b) depicts the corresponding state evolution, with the numbers corresponding to the pulse number and the arrows indicating the superposition state at the end of

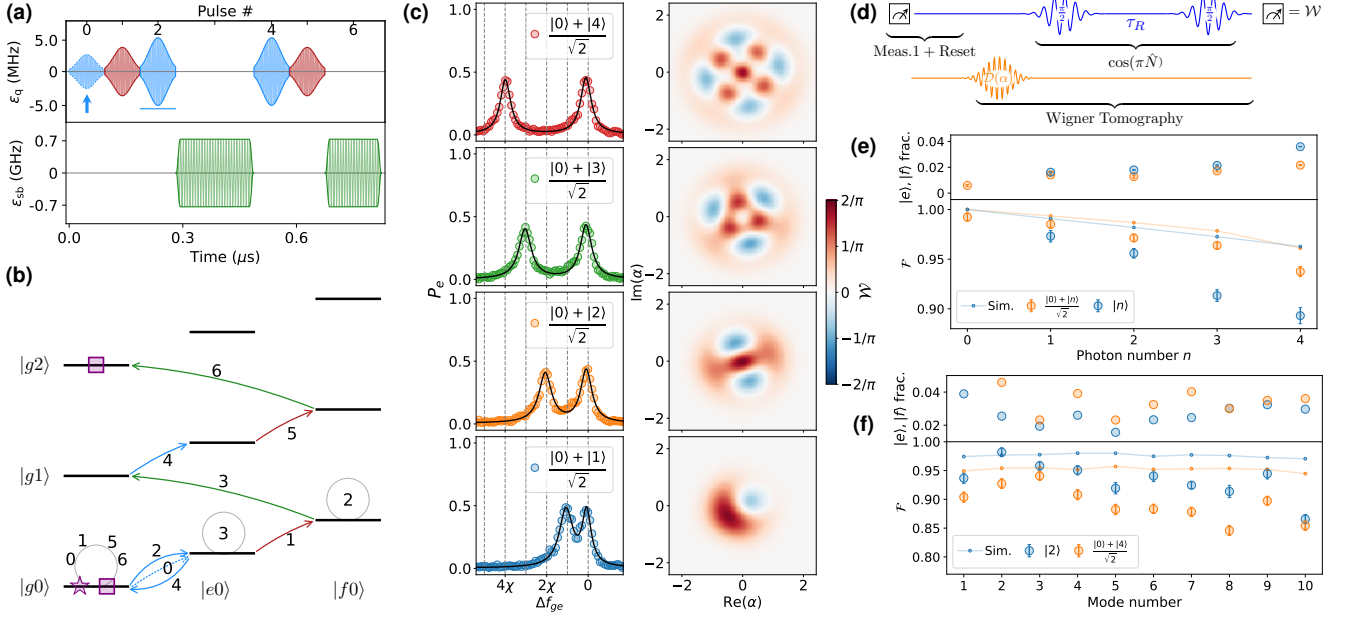


FIG. 3. **Single-mode control using transmon rotations and sideband transitions.** (a) Pulse sequence for preparing $(|0\rangle + |2\rangle)/\sqrt{2}$ in a target mode in ~ 800 ns, corresponding to $\approx \frac{1}{6\chi}$ for this mode (3). The arrow indicates the initial pulse used to prepare a transmon superposition, while the blue underline denotes a shelving pulse. An arbitrary superposition of $\cos\theta|0\rangle + e^{i\varphi}\sin\theta|n\rangle$ can be encoded by adjusting the initial transmon pulse rotation. (b) Energy level diagram representing the combined Hilbert space of the transmon and one of the cavity modes, illustrating the state transitions induced by the pulse sequence in (a). The purple star indicates the initial state, and the purple squares indicate the final superposition state. The numbers indicate the states occupied after each pulse in the sequence. The circles denote the state remaining unchanged by the corresponding pulse. (c) (Left) Photon number–resolved spectroscopy and (right) Wigner tomography of the cavity state after preparing $(|0\rangle + |n\rangle)/\sqrt{2}$ for $n = 1-4$, post-selected on the transmon being in $|g\rangle$. For the preparation of $|n\rangle$ in any cavity mode, the shelving pulses are omitted and the transmon is initialized in $|e\rangle$ with a π_{ge} pulse. (d) The pulse sequence used for Wigner tomography with post-selection, comprising an initial transmon measurement followed by a standard Wigner tomography sequence that includes a cavity displacement and subsequent parity measurement. (e) (Top) Fraction of shots not in $|g\rangle$ in the first measurement as a function of n following preparation of $|n\rangle$ and $(|0\rangle + |n\rangle)/\sqrt{2}$. (Bottom) Corresponding fidelities obtained from Wigner tomography conditioned on the transmon being in $|g\rangle$. (f) (Top) Fraction of population not in $|g\rangle$ and (bottom) Wigner tomography fidelities post-selected on the transmon being in $|g\rangle$ after preparing binomial code states in any of the cavity modes.

each pulse. By adjusting the initial transmon pulse (indicated by the blue arrow), we note that the sequence implements a unitary operation that encodes transmon superpositions into arbitrary vacuum–Fock state superpositions, $\cos\theta|0\rangle + e^{i\varphi}\sin\theta|n\rangle$.

We characterize the prepared states by performing photon-number-resolved transmon spectroscopy to obtain the Fock-state populations of the cavity state. We also use Wigner tomography to fully characterize the cavity state density matrix. These protocols assume that the transmon is in the $|g\rangle$ state and initially disentangled from the cavity. However, decoherence and coherent calibration errors can lead to residual entanglement between the transmon and cavity modes at the end of gate operations. We mitigate the resulting uncontrolled state-characterization errors by measuring the transmon before state characterization and post-selecting on outcomes where the transmon is in $|g\rangle$. To minimize the ef-

fect of cavity decoherence during the initial post-selection measurement, we implement a fast integrated readout and reset pulse [42], detailed in Section S8 C of the Supplementary Information. Figure 3(c) (left) shows the photon-number-resolved spectroscopy of the transmon, while Figure 3(c) (right) shows the corresponding reconstructed Wigner functions of the prepared superposition states up to $n = 4$, both after post-selection. The pulse sequence used for Wigner tomography with post-selection is shown in Figure 3(d).

The fidelities for Fock ($|n\rangle$) and vacuum-Fock superposition states ($(|0\rangle + |n\rangle)/\sqrt{2}$) as a function of n for mode three are shown in Figure 3(e) (bottom), with the fraction of shots not in $|g\rangle$ shown on top. Similarly, the fidelities for preparing binomial code states in any of the ten modes of the cavity, post-selected on the transmon in $|g\rangle$, are shown in Figure 3(f). The experimental results are compared with master simulations incorporating transmon

and cavity decoherence. The discrepancy is attributed to a combination of imperfect calibration of the sideband pulses, and underestimating the fidelity of the state due to noise in the Wigner tomography measurements. The error bars for the fidelities are extracted by considering both the noise in the data and the uncertainty in the parity measurement calibration. The noise in the data leads to both a spread in the reconstructed fidelity as well as a systematic lowering. The calibration and error analysis for Wigner tomography are detailed in Section S8 D of the Supplementary Information. We note that the weak dispersive coupling results in a long duration for the parity measurement ($1/(2\chi) \sim 2.5 \mu\text{s}$), and the cavity-state measurement is affected by ancilla decoherence. This can potentially be avoided in the weak coupling limit by instead measuring the characteristic function of the cavity state through conditional displacements [6, 15]. In our case, to obtain accurate state fidelities, we employ an error mitigation technique by rescaling the parity measurement to account for transmon decoherence during the parity measurement (see Section S8 A in the Supplementary Information). We also account for the reduction in contrast due to the finite bandwidth of the parity measurement.

V. MULTIMODE ENTANGLEMENT

We extend the protocol used to encode vacuum-Fock superpositions to multiple modes and prepare entangled NOON states of the form $\cos\theta|N0\rangle + e^{i\varphi}\sin\theta|0N\rangle$. The pulse sequence to implement this is shown in Figure 4(a). Shelving pulses to the $|e\rangle$ manifold (underlined in blue) ensures that sideband pulses only act on one state of the superposition at a time. The angles θ, φ are controlled by the initial transmon $|g\rangle$ - $|e\rangle$ pulse (indicated by an arrow), and the sequence following it realizes a unitary that encodes the qubit into a NOON state superposition for a cavity state starting off in the vacuum.

We first prepare symmetric maximally entangled NOON states ($\theta = \pi/2$) and characterize them using photon-number-resolved spectroscopy of the transmon, shown in Figure 4(b) (performed here without post-selection). The dispersive interaction leads to the cavity states $|N0\rangle$ and $|0N\rangle$ having peaks in the transmon spectrum that differ in frequency by $N\Delta\chi$, where $\Delta\chi$ is the difference in dispersive shifts between the two modes. The similar dispersive shifts for the modes of our system ($\Delta\chi \approx 30 \text{ kHz}$) allow us to only resolve the peaks for higher photon number NOON states ($N > 2$). However, the experiment demonstrates that the state does not have populations in other photon numbers to under 2%. To confirm the coherence of our state preparation, we perform a Ramsey-like experiment where we decode the NOON states $|N0\rangle$ and $|0N\rangle$ back to the transmon $|g\rangle$ and $|e\rangle$ states. We then apply a $\frac{\pi}{2}$ -pulse with varying phase and observe oscillations that verify the coherence of the prepared NOON states. By varying the delay time

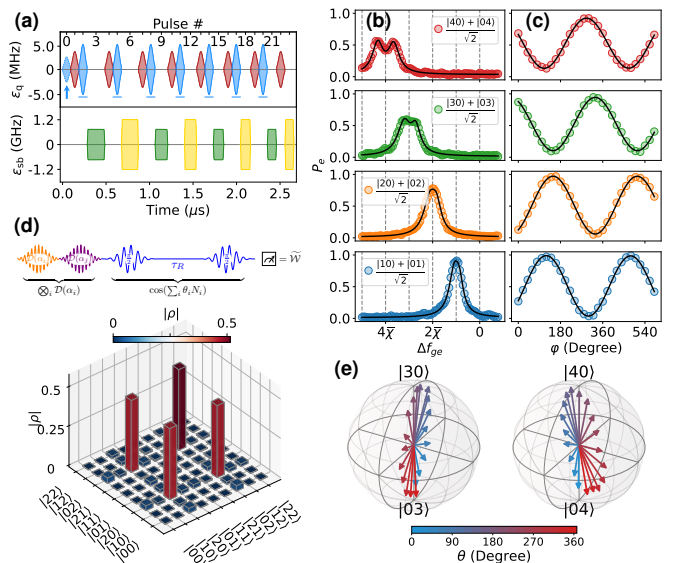


FIG. 4. Preparation and characterization of two-mode entangled states. (a) Pulse sequence for preparing a NOON state with $N = 4$. The initial pulse preparing an arbitrary transmon $|g\rangle$ - $|e\rangle$ superposition is indicated by an arrow while the blue underlines indicate the shelving pulses. (b) Photon-number-resolved spectroscopy of NOON states (between modes three and five) up to $N = 4$. $\bar{\chi}$ is the average dispersive shift of the two modes. (c) Coherence of the NOON state measured using a $\pi/2$ pulse with varying phase after decoding the NOON state back to the transmon $|g\rangle$ - $|e\rangle$ subspace. (d) The density matrix of a NOON state ($N = 2$) extracted using multimode Wigner tomography (e) Tomography of $|\psi\rangle = \cos\theta|N0\rangle + e^{i\varphi}\sin\theta|0N\rangle$ versus θ within the NOON state subspace, for $N = 3, 4$. This was measured by decoding the NOON state back into the transmon $|g\rangle$ - $|e\rangle$ subspace and performing qubit tomography.

between the encode and the decode operations, we can measure the decay time of the NOON state, finding it to be $1.27 \pm 0.05 \text{ ms}$ for $N = 1$ (see Section S10 of the Supplementary Information).

Additionally, we characterize NOON states up to $N = 2$ using multimode Wigner tomography [8, 43]. This is implemented through the pulse sequence shown in Figure 4(d) (top) by displacing both cavities to a set of chosen displacements and measuring a generalized parity-like operator $\tilde{\Pi} = \cos(\theta_1\hat{n}_1 + \theta_2\hat{n}_2)$, where \hat{n}_i is the photon number in mode i . The measurement of $\tilde{\Pi}$ is performed through a transmon Ramsey experiment with delay time τ_R , so that $\theta_i = \chi_i\tau_R \approx \pi$. The density matrix is then obtained by inverting the measurements while enforcing physicality constraints. The result for $N = 2$ is shown in Figure 4(d) (bottom). We extract post-selected fidelities of $\mathcal{F} = 0.95 \pm 0.012$ and $\mathcal{F} = 0.905 \pm 0.012$ for NOON states with $N = 1$ and 2, respectively. Lastly, we verify that we can accurately prepare any state within the $\{|N0\rangle, |0N\rangle\}$ subspace by varying the amplitude and

phase of the initial transmon pulse, decoding the state, and subsequently performing qubit tomography. We visualize the resulting states on the $\{|N0\rangle, |0N\rangle\}$ Bloch sphere, as shown in Figure 4(e) for $N = 3, 4$. This confirms the expected trajectory and the ability to prepare the state at an arbitrary point in the encoded NOON state subspace.

The space of two-mode superposition states that can be realized with sideband transitions and transmon rotations, by shelving in the $|e\rangle$ manifold, is restricted to basis states of the form $\{|n0\rangle, |0p\rangle\}$. We introduce a second control technique that allows for the implementation of unitary operations that encode arbitrary multimode Fock states $\{|n_1n_2\dots\rangle, |p_1p_2\dots\rangle\}$, as shown in Section S4 of the Supplementary Information. This method addresses the challenge of realizing gates amid incommensurate sideband transition rates across different photon numbers by leveraging the residual dispersive interaction, which is not available on other hardware platforms, such as trapped ions and mechanical resonators. As shown in Figure 2(b), the dispersive interaction causes sideband transitions corresponding to different photon numbers ($|f, n\rangle \rightarrow |g, n+1\rangle$) to vary in frequency by $n\chi_f$. These dispersive shifts allow us to use the detuning of the sideband drive as a control parameter to synchronize transitions for different photon numbers. This enables *photon-number-selective* (PNS) sideband transitions, where we perform a π pulse on a specific photon number while effectively performing no transition (e.g., 2π rotation) on another state. This technique is similar to those applied in other superconducting gate protocols [11, 44].

VI. SIDEBAND-BASED ENCODING UNITARY FOR THE BINOMIAL CODE

We demonstrate our new method of unitary synthesis by implementing an encoding gate for the binomial code—an operation that maps an arbitrary qubit in the transmon $|g\rangle$ - $|e\rangle$ subspace, $u|g\rangle + v|e\rangle$, onto a corresponding superposition of binomial code states, $u|2\rangle + v\frac{|0\rangle+|4\rangle}{\sqrt{2}}$. While this unitary has previously been demonstrated in the strong-dispersive regime [14, 16] (with $\chi \sim 2$ MHz), we demonstrate a fast encoding gate in the weak-dispersive regime with nearly an order of magnitude smaller χ than in previous demonstrations. We implement our sideband-based binomial encoding unitary using the pulse sequence shown in Figure 5(a). The sequence is again composed entirely of sideband and transmon rotations, with the key addition of two PNS sidebands, marked by the black arrows. The state transitions effected by the PNS sidebands (following pulse 13 of the sequence) are illustrated in the energy level diagram in Figure 5(b). The complete sequence of state transitions for both $|g0\rangle$ and $|e0\rangle$ input states is provided in Fig. S15 of the Supplementary Information.

In our scheme, the PNS sidebands are crucial for separating different cavity Fock states (e.g., $|g2\rangle$ and $|g4\rangle$)

into distinct transmon manifolds, enabling these states to be addressed either simultaneously with transmon pulses or independently with fast, unselective sideband pulses through the use of shelving. Specifically, the two PNS sidebands perform a π -pulse for the $|f1\rangle \leftrightarrow |g2\rangle$ and $|f0\rangle \leftrightarrow |g1\rangle$ transitions, while implementing 2π and 4π rotations, respectively, for the $|f3\rangle \leftrightarrow |g4\rangle$ transition. These selective sidebands are the rate-limiting steps of the operation, scaling with the dispersive interaction but benefiting from favorable scaling factors due to their dependence on the dispersive shift of the $|f\rangle$ state and the involvement of higher photon numbers in the binomial code (see Section S9 of the Supplementary Information). With this, we implement the binomial encoding gate in a time shorter than the timescale set by the $|e\rangle$ dispersive shift, $1/\chi_e$, making the gate fast in an intermediate- χ regime where Purcell-limited cavity lifetimes can still be long. This gate speed can be further enhanced by using the transmon straddling regime [45] to enhance χ_f without a commensurate increase in cavity Purcell decay. In our work, the inverse-Purcell-limited cavity lifetime is approximately 60 ms, which is comparable to the best reported lifetimes in niobium-based cavities [18–20].

We characterize the unitary gate by performing Wigner tomography of the cavity states following the encoding operation, after initializing the transmon at six cardinal points on the transmon $|g\rangle$ - $|e\rangle$ Bloch sphere, as shown in Figure 5(e). The Wigner tomography is implemented with post-selection to characterize the cavity state accurately. The resulting states are consistent with expectations and are further verified by photon-number-resolved spectroscopy of the transmon, shown in Figure 5(f), which displays peaks corresponding to the expected even Fock states, with populations consistent with those extracted from Wigner tomography to $\sim 2\%$. We illustrate the encoded unitary by projecting the density matrices extracted from Wigner tomography into the subspace of binomial code states and reconstructing the states in the Bloch sphere of logical qubit, as shown in Figure 5(g). The fraction of the shots with the transmon not in $|g\rangle$ range from 8–9% as shown in Figure 5(h) (top). The post-selected fidelities (on $|g\rangle$) for the different fiducial states are shown in Figure 5(h) (bottom) and range from 95.6–96.9%. These results are consistent with master equation simulations (see Section S9 in the Supplementary Information) and are near the coherence limit. The detailed error budget for the Binomial encoding gate is shown in Fig. S17 of the Supplementary Information. We find the gate infidelity to be dominated by ancilla decoherence, even for the post-selected fidelities. With state-of-the-art transmon coherence times ($T_1, T_\varphi = 500, 200 \mu\text{s}$), we expect post-selected $|g\rangle$ fractions of 0.3% and binomial encode fidelities of $\geq 99\%$ without post selection. The fidelities can also be improved by using mid-circuit measurements and feed-forward. These can be selectively implemented only for the slower PNS sidebands to significantly reduce infidelity.

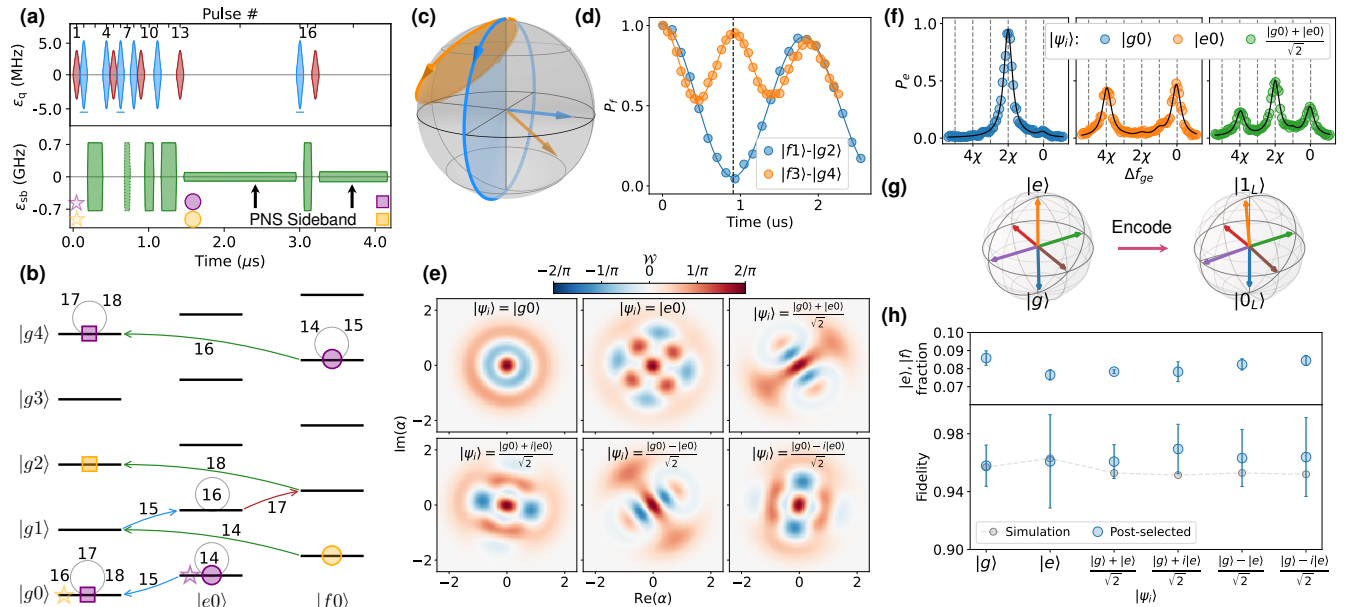


FIG. 5. **Unitary encoding operation for the binomial code.** (a) Pulse sequence for an encoding operation which maps transmon states to binomial code states ($|g\rangle \rightarrow |2\rangle$ and $|e\rangle \rightarrow (|0\rangle + |4\rangle)/\sqrt{2}$). The rate-limiting photon-number-selective (PNS) sidebands are indicated by the arrows and the shelving pulses are indicated by underlines. (b) Energy level diagram of the combined Hilbert space of the transmon and a cavity mode. The gold circles represent the state after pulse 13 of the encoding sequence for the initial state of $|g0\rangle$ (gold star), and the purple circle corresponds to the initial state of $|e0\rangle$ (purple star). The subsequent pulses use PNS sidebands to bring the state back onto the $|g\rangle$ manifold of the transmon, completing the encoding gate. State transitions are tracked by arrows, while the gray circles denote no state change for that particular superposition branch during a given pulse. The final binomial code states are indicated by purple and orange squares. Numbers indicate the states occupied at the end of each corresponding pulse in the sequence. (c) Bloch sphere illustration showing the principle of PNS sidebands, with a π rotation applied to the target transition and cycling of the second transition. (d) Rabi oscillations for the $|f1\rangle \leftrightarrow |g2\rangle$ and $|f3\rangle \leftrightarrow |g4\rangle$ transitions, showing the timing for a π and 2π rotation, respectively, corresponding to pulse 18 of the encoding sequence. (e) Reconstructed Wigner functions of the cavity states after the encoding operation, demonstrating the preparation of corresponding binomial code states when the transmon is initialized in six cardinal states. (f) Photon-number-resolved spectroscopy of the prepared Binomial code states. (g) Bloch sphere representation of the encoding operation, illustrating the transition from the transmon Bloch sphere to the logical binomial code Bloch sphere. (h) (Top) The fraction of the population not in $|g\rangle$ after the encoding operation for six cardinal transmon states. (Bottom) Wigner tomography fidelities of the binomial code states following the encoding operation (blue markers) compared against the expected fidelities from Lindblad master equation simulations (gray markers).

VII. CONCLUSION

In summary, we have used transmon-mediated charge-driven sideband interactions to demonstrate fast sideband control of a weakly coupled multimode bosonic memory. We achieve transmon-cavity SWAP gates in 10 modes in 150–350 ns, which is 15–30 times faster than the bare dispersive coupling. Using this, we implement a tunable Jaynes–Cummings interaction within the transmon $\{|g\rangle, |f\rangle\}$ subspace and introduce two strategies to address challenges associated with implementing unitary gates: a shelving technique that prevents unwanted transitions by temporarily storing populations in the sideband-transparent $|e\rangle$ manifold of the transmon, and exploiting the dispersive shift to synchronize sideband transition to implement photon-number-selective sideband gates. Using this, we demonstrated

few-microsecond gates that encode a qubit into vacuum-Fock superposition in arbitrary modes and NOON states in arbitrary pairs of modes. Our encoding protocol is straightforwardly generalizable to arbitrary multimode Fock encodings. In addition, we have also prepared binomial code states across ten cavity modes. Finally, we implemented a new binomial encoding gate with average fidelities of 96.3% for the encoded binomial states after post-selection. This gate is executed in approximately 4 μ s, comparable with previous demonstrations, but with a bare dispersive coupling that is an order of magnitude weaker.

The shelving techniques introduced in this work can be extended to implement a larger space of gates by using higher transmon states [46, 47]. For example, access to the $|h\rangle$ state allows for autonomous error correction following a controlled-parity gate for the binomial code.

The techniques presented in this work are highly relevant for implementing fast sideband-based gate operations in quantum processors and memories comprised of state-of-the-art ultra-low-loss niobium cavities without spoiling cavity coherence [48]. While building a multimode random-access memory requires fixing many-body coherent errors with new random-access architectures [49], the large contrast between the speed of sideband gates and the bare dispersive shift that we have demonstrated can potentially allow for their mitigation through frequency-robust sideband and transmon pulses [22] and dynamical decoupling. Our control techniques allow for efficient control of multiple logical qubits in our multimode memory and tests of gate operations, code concatenation, and multimode bosonic codes [50–52]. Our results provide a promising path toward fast bosonic unitary operations in multimode circuit QED systems, addressing key challenges in bosonic quantum error correction and quantum computing.

ACKNOWLEDGEMENTS

We are grateful for insightful discussions with David Schuster, Michael Gershenson, Jens Koch, Tanay Roy, Xinyuan You, Taeyoon Kim, Shyam Shankar, Wolfgang Pfaff, Angela Kou, and Yuan Liu. We acknowledge Cole Woloszyn and Paul Pickard of the Rutgers Physics and Astronomy Machine Shop for the cavity fabrication. We acknowledge David Schuster, Connie Miao, and Sara Sussman for their support in setting up the QICK measurement hardware; Taekwan Yoon and Zhixin Wang for the setup of Zurich instruments hardware; and David Van Zaanten, Alexander Romanenko, and Anna Grassellino for their support in transmon fabrication. We sincerely thank Michael Gershenson for providing access to his laboratory space and appreciate the support of Michael Gershenson, Plamen Kamenov, Ethan Kasaba, Andre Barbosa, and Raymond Niu in setting up the dilution refrigerator and microwave hardware used in these measurements.

This work is supported by the U.S. Department of Energy, Office of Science and National Quantum Information Science Research Centers, Superconducting Quantum Materials and Systems Center (SQMS) under contract number DE-AC02-07CH11359, and by the Army Research Office under Grant Number W911NF-23-1-0096 and W911NF-23-1-0251.

-
- [1] A. Wallraff, D. I. Schuster, A. Blais, L. Frunzio, R.-S. Huang, J. Majer, S. Kumar, S. M. Girvin, and R. J. Schoelkopf, *Nature* **431**, 162 (2004).
- [2] M. Reagor, W. Pfaff, C. Axline, R. W. Heeres, N. Ofek, K. Sliwa, E. Holland, C. Wang, J. Blumoff, K. Chou, *et al.*, *Physical Review B* **94**, 014506 (2016).
- [3] R. Naik, N. Leung, S. Chakram, P. Groszkowski, Y. Lu, N. Earnest, D. McKay, J. Koch, and D. Schuster, *Nature Communications* **8**, 1904 (2017).
- [4] S. Chakram, A. E. Oriani, R. K. Naik, A. V. Dixit, K. He, A. Agrawal, H. Kwon, and D. I. Schuster, *Physical Review Letters* **127**, 107701 (2021).
- [5] R. W. Heeres, P. Reinhold, N. Ofek, L. Frunzio, L. Jiang, M. H. Devoret, and R. J. Schoelkopf, *Nature Communications* **8**, 94 (2017).
- [6] A. Eickbusch, V. Sivak, A. Z. Ding, S. S. Elder, S. R. Jha, J. Venkatraman, B. Royer, S. M. Girvin, R. J. Schoelkopf, and M. H. Devoret, *Nature Physics* **18**, 1464 (2022).
- [7] C. Wang, Y. Y. Gao, P. Reinhold, R. W. Heeres, N. Ofek, K. Chou, C. Axline, M. Reagor, J. Blumoff, K. Sliwa, *et al.*, *Science* **352**, 1087 (2016).
- [8] S. Chakram, K. He, A. V. Dixit, A. E. Oriani, R. K. Naik, N. Leung, H. Kwon, W.-L. Ma, L. Jiang, and D. I. Schuster, *Nature Physics* **18**, 879 (2022).
- [9] S. Rosenblum, Y. Y. Gao, P. Reinhold, C. Wang, C. J. Axline, L. Frunzio, S. M. Girvin, L. Jiang, M. Mirrahimi, M. H. Devoret, *et al.*, *Nature communications* **9**, 652 (2018).
- [10] Y. Y. Gao, B. J. Lester, K. S. Chou, L. Frunzio, M. H. Devoret, L. Jiang, S. Girvin, and R. J. Schoelkopf, *Nature* **566**, 509 (2019).
- [11] B. J. Chapman, S. J. de Graaf, S. H. Xue, Y. Zhang, J. Teoh, J. C. Curtis, T. Tsunoda, A. Eickbusch, A. P. Read, A. Koottandavida, *et al.*, *PRX Quantum* **4**, 020355 (2023).
- [12] Y. Lu, A. Maiti, J. W. Garmon, S. Ganjam, Y. Zhang, J. Claes, L. Frunzio, S. M. Girvin, and R. J. Schoelkopf, *nature communications* **14**, 5767 (2023).
- [13] N. Ofek, A. Petrenko, R. Heeres, P. Reinhold, Z. Leghtas, B. Vlastakis, Y. Liu, L. Frunzio, S. Girvin, L. Jiang, *et al.*, *Nature* **536**, 441 (2016).
- [14] L. Hu, Y. Ma, W. Cai, X. Mu, Y. Xu, W. Wang, Y. Wu, H. Wang, Y. Song, C.-L. Zou, *et al.*, *Nature Physics* **15**, 503 (2019).
- [15] P. Campagne-Ibarcq, A. Eickbusch, S. Touzard, E. Zalysgeller, N. E. Frattini, V. V. Sivak, P. Reinhold, S. Puri, S. Shankar, R. J. Schoelkopf, *et al.*, *Nature* **584**, 368 (2020).
- [16] Z. Ni, S. Li, X. Deng, Y. Cai, L. Zhang, W. Wang, Z.-B. Yang, H. Yu, F. Yan, S. Liu, *et al.*, *Nature* **616**, 56 (2023).
- [17] V. V. Sivak, A. Eickbusch, B. Royer, S. Singh, I. Tsioutsios, S. Ganjam, A. Miano, B. Brock, A. Ding, L. Frunzio, *et al.*, *Nature* **616**, 50 (2023).
- [18] A. Romanenko, R. Pilipenko, S. Zorzetti, D. Frolov, M. Awida, S. Belomestnykh, S. Posen, and A. Grassellino, *Physical Review Applied* **13**, 034032 (2020).
- [19] O. Milul, B. Guttel, U. Goldblatt, S. Hazanov, L. M. Joshi, D. Chausovsky, N. Kahn, E. Çiftyürek, F. Lafont, and S. Rosenblum, *PRX Quantum* **4**, 030336 (2023).

- [20] A. E. Oriani, F. Zhao, T. Roy, A. Anferov, K. He, A. Agrawal, R. Banerjee, S. Chakram, and D. I. Schuster, arXiv preprint arXiv:2403.00286 <https://doi.org/10.48550/arXiv.2403.00286> (2024).
- [21] I. Pietikäinen, O. Černotík, A. Eickbusch, A. Maiti, J. W. Garmon, R. Filip, and S. M. Girvin, PRX Quantum **5**, 040307 (2024).
- [22] X. You, Y. Lu, T. Kim, D. M. Kurkcuolu, S. Zhu, D. Van Zanten, T. Roy, Y. Lu, S. Chakram, A. Grassellino, *et al.*, Physical Review Applied **22**, 044072 (2024).
- [23] R. W. Heeres, B. Vlastakis, E. Holland, S. Krastanov, V. V. Albert, L. Frunzio, L. Jiang, and R. J. Schoelkopf, Physical review letters **115**, 137002 (2015).
- [24] L. Bretheau, P. Campagne-Ibarcq, E. Flurin, F. Mallet, and B. Huard, Science **348**, 776 (2015).
- [25] A. A. Diring, E. Blumenthal, A. Grinberg, L. Jiang, and S. Hacoen-Gourgy, Phys. Rev. X **14**, 011055 (2024).
- [26] A. Wallraff, D. Schuster, A. Blais, J. Gambetta, J. Schreier, L. Frunzio, M. Devoret, . f. S. Girvin, and R. Schoelkopf, Physical Review Letters **99**, 050501 (2007).
- [27] W. Pfaff, C. J. Axline, L. D. Burkhardt, U. Vool, P. Reinhold, L. Frunzio, L. Jiang, M. H. Devoret, and R. J. Schoelkopf, Nature Physics **13**, 882 (2017).
- [28] Y. Y. Gao, B. J. Lester, Y. Zhang, C. Wang, S. Rosenblum, L. Frunzio, L. Jiang, S. Girvin, and R. J. Schoelkopf, Physical Review X **8**, 021073 (2018).
- [29] M. Mollenhauer, A. Irfan, X. Cao, S. Mandal, and W. Pfaff, arXiv preprint arXiv:2407.16743 <https://doi.org/10.48550/arXiv.2407.16743> (2024).
- [30] M. Pechal, L. Huthmacher, C. Eichler, S. Zeytinoglu, A. Abdumalikov Jr, S. Berger, A. Wallraff, and S. Filipp, Physical Review X **4**, 041010 (2014).
- [31] C. K. Law and J. H. Eberly, Phys. Rev. Lett. **76**, 1055 (1996).
- [32] A. Ben-Kish, B. DeMarco, V. Meyer, M. Rowe, J. Britton, W. M. Itano, B. Jelenković, C. Langer, D. Leibfried, T. Rosenband, *et al.*, Physical review letters **90**, 037902 (2003).
- [33] M. Hofheinz, H. Wang, M. Ansmann, R. C. Bialczak, E. Lucero, M. Neeley, A. O'connell, D. Sank, J. Wenner, J. M. Martinis, *et al.*, Nature **459**, 546 (2009).
- [34] Y. Liu, J. Sinanan-Singh, M. T. Kearney, G. Mintzer, and I. L. Chuang, Physical Review A **104**, 032605 (2021).
- [35] N. Khaneja, T. Reiss, C. Kehlet, T. Schulte-Herbrüggen, and S. J. Glaser, Journal of Magnetic Resonance **172**, 296 (2005).
- [36] T. Fösel, S. Krastanov, F. Marquardt, and L. Jiang, arXiv preprint arXiv:2004.14256 <https://doi.org/10.48550/arXiv.2004.14256> (2020).
- [37] M. Kudra, M. Kervinen, I. Strandberg, S. Ahmed, M. Scigliuzzo, A. Osman, D. P. Lozano, M. O. Tholén, R. Borgani, D. B. Haviland, *et al.*, PRX Quantum **3**, 030301 (2022).
- [38] M. H. Michael, M. Silveri, R. Brierley, V. V. Albert, J. Salmilehto, L. Jiang, and S. M. Girvin, Physical Review X **6**, 031006 (2016).
- [39] S. Zeytinoglu, M. Pechal, S. Berger, A. A. Abdumalikov, A. Wallraff, and S. Filipp, Phys. Rev. A **91**, 043846 (2015).
- [40] R. Shillito, A. Petrescu, J. Cohen, J. Beall, M. Hauru, M. Ganahl, A. G. Lewis, G. Vidal, and A. Blais, Phys. Rev. Appl. **18**, 034031 (2022).
- [41] X. Jin, A. Kamal, A. Sears, T. Gudmundsen, D. Hover, J. Miloshi, R. Slattery, F. Yan, J. Yoder, T. Orlando, *et al.*, Physical Review Letters **114**, 240501 (2015).
- [42] D. T. McClure, H. Paik, L. S. Bishop, M. Steffen, J. M. Chow, and J. M. Gambetta, Physical Review Applied **5**, 011001 (2016).
- [43] K. He, M. Yuan, Y. Wong, S. Chakram, A. Seif, L. Jiang, and D. I. Schuster, Nature communications **15**, 4138 (2024).
- [44] T. Tsunoda, J. D. Teoh, W. D. Kalfus, S. J. de Graaf, B. J. Chapman, J. C. Curtis, N. Thakur, S. M. Girvin, and R. J. Schoelkopf, PRX Quantum **4**, 020354 (2023).
- [45] J. Koch, T. M. Yu, J. Gambetta, A. A. Houck, D. I. Schuster, J. Majer, A. Blais, M. H. Devoret, S. M. Girvin, and R. J. Schoelkopf, Physical Review A—Atomic, Molecular, and Optical Physics **76**, 042319 (2007).
- [46] Z. Wang, R. W. Parker, E. Champion, and M. S. Blok, arXiv preprint arXiv:2407.17407 <https://doi.org/10.48550/arXiv.2407.17407> (2024).
- [47] S. Rosenblum, P. Reinhold, M. Mirrahimi, L. Jiang, L. Frunzio, and R. Schoelkopf, Science **361**, 266 (2018).
- [48] Y. Lu, T. Kim, T. Roy, X. You, O. V. Pronitchchev, M. Bal, S. Garattoni, F. Crisa, D. Bafia, R. M. Pilipenko, P. Heidler, A. C. Y. Li, Y. Lu, D. van Zanten, S. Zorzetti, R. Harnik, A. Murthy, S. Zhu, A. Vallières, Z. Huang, J. Koch, A. Grassellino, S. Chakram, and A. Romanenko, Bull. Am. Phys. Soc. (2025).
- [49] R. Banerjee, S. Chakram, A. Oriani, F. Zhao, K. He, A. Agrawal, and D. Schuster, Bull. Am. Phys. Soc. (2022).
- [50] I. L. Chuang, D. W. Leung, and Y. Yamamoto, Physical Review A **56**, 1114 (1997).
- [51] V. V. Albert, S. O. Mundhada, A. Grimm, S. Touzard, M. H. Devoret, and L. Jiang, Quantum Science and Technology **4**, 035007 (2019).
- [52] B. Royer, S. Singh, and S. Girvin, PRX Quantum **3**, 010335 (2022).